

Ultrahigh-Ni Cathode with Superior Structure Stability Enabled by a Covalent Bonding Strategy

Caihu Li,^[a, b] Xudong Zhang,^[a] Yichao Cui,^[a, b] Yanan Xu,^[a] Xiong Zhang,^[a, b] Xianzhong Sun,^[a, b] Kai Wang,*^[a, b] and Yanwei Ma*^[a, b, c]

Ultrahigh-nickel layered oxide cathodes are the most promising cathode materials for high-energy lithium-ion batteries. However, the rapid structural degradation during cycling charge-discharge process limits its commercial application. Herein, we report a covalent pinning strategy to enhance structure stability of ultrahigh-Ni cathode $\text{LiNi}_{0.9}\text{Co}_{0.06}\text{Mn}_{0.04}\text{O}_2$ (NCM90). Zr is gradient diffused into the lattice of NCM90 and forms Zr–O bonds during the sintering process, which can effectively alleviate the lattice distortion like introducing pinning centers due to the stronger bond energy, enhancing its structure stability during charge-discharge process. In the meanwhile, the

Zr–O on the surface of NCM90 powder forms $\text{Li}_x\text{Zr}_y\text{O}_z$ coating layer due to the reaction with lithium residue, which prevents from the edge reconstruction and mitigates the occurrence of side reactions, as well as ensuring a fast Li^+ diffusion pathway crossing the interface. As a result, the Zr–O modified NCM90 (Zr-NCM) achieves 88.8% remarkable capacity retention at 1 C after 200 cycles over 2.8–4.3 V, which is superior to the pristine NCM90 with 71.2% retention. This work demonstrates that the Zr–O bonding can provide an effective structure pinning for the ultrahigh-Ni cathode, which will largely guide the development of high-performance lithium-ion battery cathode materials.

Introduction

The development of the electric vehicle industry has put forward increasing requirements for the energy density of lithium-ion batteries (LIBs). The cathode is not only the lithium source, but also the critical part that determines the energy density of lithium-ion batteries.^[1,2] LiCoO_2 , $\text{LiNi}_x\text{Co}_y\text{Mn}_z\text{O}_2$ (NCM) and LiFePO_4 are the three most employed cathode materials for commercial LIBs.^[3] Among them, the Ni-rich layered cathode ($\text{LiNi}_x\text{Co}_y\text{Mn}_z\text{O}_2$ with the $x \geq 0.6$) is attracting attention due to its large capacity and high discharge platform, which is considered as the most promising cathode for high energy-density lithium-ion batteries.

In NCM materials, nickel is generally bivalent and its electronic configuration is $t_{2g}^6e_g^2$. Compared to trivalent cobalt ($t_{2g}^6e_g^0$) and tetravalent manganese ($t_{2g}^3e_g^0$), there are two electrons that can transfer at the e_g levels of nickel, which has a higher energy than the t_{2g} levels due to the increased electrostatic repulsion of the coordination anion. Thus, the

oxidation occurs first during the charging process is Ni^{2+} to Ni^{3+} , followed by the Ni^{3+} to Ni^{4+} , and then is the oxidation of Co^{3+} to Co^{4+} .^[4–6] Consequently, nickel primarily plays a role in providing capacity in NCM materials, and more nickel means larger energy density. However, with the increase of nickel content, the structural stability of NCM materials gradually decreases,^[7,8] owe to the following three reasons.^[9,10] (1) Cation mixing. With similar ionic radius, Ni^{2+} (0.069 nm) tends to enter the Li^+ (0.076 nm) layer and occupies the Li^+ site during synthesis process and the whole life of the battery, leading to the structure transform of LiMO_2 from the $\text{R}\bar{3}\text{m}$ to the $\text{Fm}\bar{3}\text{m}$. In the meanwhile, the large attraction of Ni^{2+} to the adjacent oxygen atoms (Ni–O) will increase the diffusion activation energy barrier of lithium ions. As a result, the capacity and rate performance of Ni-rich layered cathode materials deteriorate. It is notable that the degree of cation mixing will increase following the increases of Ni content.^[11–13] (2) Irreversible phase transformation and micro-cracks. Nickel ions gradually migrate from lattice to the surface along the diffusion direction of lithium ions, and finally dissolve into electrolyte during cycling, thus resulting in a rearrangement of atoms and an electrochemical inert transformation of the material structure, which brings about a continuous deterioration of electrochemical performance.^[14] Additionally, lattice strain is inevitable during the charging and discharging of the Ni-rich layered cathodes, because the radius of redox ions and the coulomb repulsion of oxygen will change with the extraction and insertion of lithium ions. And the accumulation of anisotropic lattice strain can lead to the generation of propagating cracks inside electrode particles.^[15,16] (3) Surface side reactions. The presence of residual lithium compounds on the surface of the Ni-rich layered cathode is unavoidable owe to the excess LiOH involved in the synthesis process. These insulated lithium compounds (LiOH , Li_2CO_3 , etc.) not only hinder the diffusion of Li^+ , but also lead to

[a] C. Li, X. Zhang, Y. Cui, Y. Xu, X. Zhang, X. Sun, K. Wang, Y. Ma
Institute of Electrical Engineering,
Chinese Academy of Sciences
Beijing 100190, P. R. China
E-mail: wangkai@mail.iee.ac.cn
ywma@mail.iee.ac.cn

[b] C. Li, Y. Cui, X. Zhang, X. Sun, K. Wang, Y. Ma
School of Engineering Sciences,
University of Chinese Academy of Sciences
Beijing 100049, P. R. China

[c] Y. Ma
School of Materials Science and Engineering,
Zhengzhou University
Zhengzhou 450001, P. R. China

 Supporting information for this article is available on the WWW under
<https://doi.org/10.1002/batt.202400218>

a decrease in coulombic efficiency.^[17,18] Furthermore, high-valence Ni ions catalyze the decomposition of electrolyte and aggravate the transition metal dissolution, causing capacity loss and safety concerns.^[19]

Consequently, many strategies have been taken to improve the structural stability of nickel-rich cathode materials, including element doping,^[20,21] surface coating,^[22,23] hybrid structure designing,^[24] and grain size regulation.^[25] Element doping enhances the performance of NCM material by stabilizing lattice structure and accelerating ion transport, while surface coating effectively isolates the active electrode material from the electrolyte, suppressing the occurrence of side reaction that can promote the surface degradation.^[26] The combination of multiple modification strategies is the key to preparing high-performance Ni-rich electrode materials for high-energy LIBs.^[22] Benefiting from the similar ion radius to Li⁺, the Zr⁴⁺ (0.072 nm) doping has been widely used to decorate cathode materials, which can suppress cation mixing, enhance Li⁺ transport kinetics, and improve structural stability. Yao et al. synthesized Zr-doped NCM622 with 91.6% capacity retention after 100 cycles at 2C between 2.8 and 4.5 V.^[27] He et al. reported a Zr gradient doped NCM811 with a capacity retention of 83.2% after 200 cycles at 1C at 2.8–4.5 V.^[28] However, there have been few reports on the Zr doping for ultrahigh nickel NCM ($\text{LiNi}_x\text{Co}_y\text{Mn}_z\text{O}_2$ with the $x \geq 0.9$), and the mechanism of Zr⁴⁺ in ultra-high nickel positive electrode materials remains unclear.

Herein, we propose a covalent pinning strategy to enhance the stability of $\text{LiNi}_{0.9}\text{Co}_{0.06}\text{Mn}_{0.04}\text{O}_2$ (NCM90) by introducing

Zr–O bonding in both surface and bulk phase of NCM90. As shown in Figure S1, $\text{ZrO}(\text{NO}_3)_2 \cdot x\text{H}_2\text{O}$ is mixed and sintered with oxide precursor and LiOH in a sintering process, in which the Zr⁴⁺ diffuses into the bulk of NCM90. Due to the stronger bond energy of Zr–O than that of TM–O (TM=Ni, Co, Mn), the introduction of Zr–O bonding like forming pinning centers can largely enhance the lattice stability. The Zr–O bonds naked on the surface^[4] would be converted to $\text{Li}_x\text{Zr}_y\text{O}_z$ coating layer due to the reaction with LiOH in sintering process. The $\text{Li}_x\text{Zr}_y\text{O}_z$ fast ionic conductor layer can improve the kinetics and inhibit the occurrence of side reactions. As a result, the modified cathode delivers a discharge specific capacity of 201.8 mAh/g in the initial cycle between 2.8 and 4.3 V at 0.1 C ($1\text{C}=200\text{ mA g}^{-1}$), as well as a capacity retention of 88.8% after 200 cycles at 1C and 94.2% after 100 cycles at 0.5C over 2.8–4.3 V, comparatively.

Results and Discussion

The Zr incorporated NCM90 (Zr-NCM) power was prepared via a sintering process of the oxide precursor, $\text{ZrO}(\text{NO}_3)_2 \cdot x\text{H}_2\text{O}$ and LiOH. The structure topography and morphology of the NCM90 and Zr-NCM sample is shown in Figure 1a,b. The Zr-NCM shows a micron-sized spheroidal morphology composed of nanoscale primary particles, which is similar to the pristine NCM90. It is worth mentioning that the Zr-NCM shows more uniform primary particles compared to NCM90 with rod-shaped primary particles. From the EDS mapping of the Zr-NCM shown in

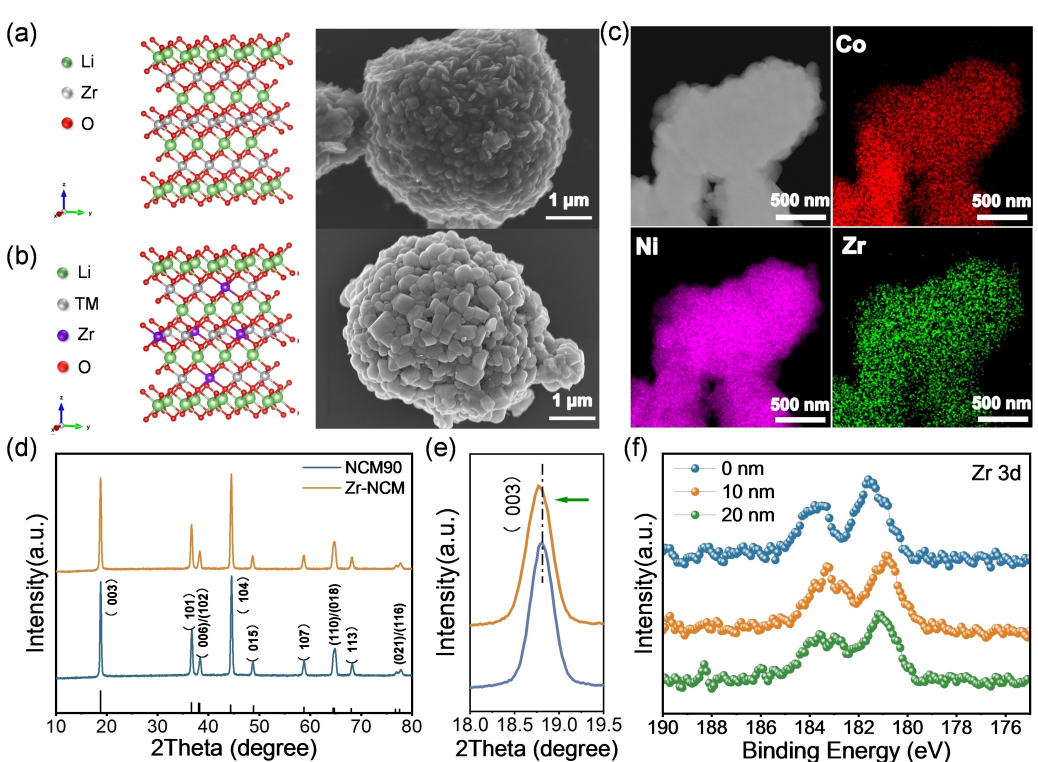


Figure 1. The crystal structures and SEM images of NCM90 (a) and Zr-NCM (b). EDS elemental mapping of Ni, Co, Zr elements (c). XRD patterns (d) with magnified views of (003) peaks (e). (f) XPS pattern of Zr 3d etched at different depths.

Figure 1c, Zr element is uniformly distributed in the entire Zr-NCM powder, indicating a uniformly Zr doping in NCM90.

To obtain information about the crystal structure, XRD patterns of the samples were collected (Figure 1d). NCM90 and Zr-NCM samples both exhibit high crystallinity. All characteristic peaks belong to the hexagonal layered $\alpha\text{-NaFeO}_2$ phase with the R-3 m space group, without additional peaks from impurities, demonstrating that the trace amounts of Zr doping has no significant effect toward the bulk structure of the NCM90.^[29] The splitting of the (006)/(102) and (108)/(110) peaks implies an orderly arranged layered structure of the prepared samples.^[30] The characteristic peak (003) of the Zr-NCM shifts significantly to lower angles (Figure 1e), and the degree of movement

increases with the increment of the Zr source (Figure S2), indicating the *c*-axis expansion caused by the intercalation of additional Zr^{4+} embedded in the lattice, which confirms the successful doping of Zr^{4+} . Subsequently, Zr 3d XPS was checked to detect the elemental composition of Zr-NCM. As shown in the Figure 1f, the signals of the Zr element appear in the different depth of the Zr-NCM powder with an etching process, which means the Zr element is not only present on the surface of the particles, but also inside the bulk phase.

To further disclose the crystallographic information, Rietveld refinements of XRD patterns were performed in Figure 2a,b, and the related parameters for the both samples are listed in Table S1. The results show that the lattice parameters *c* and *a* of

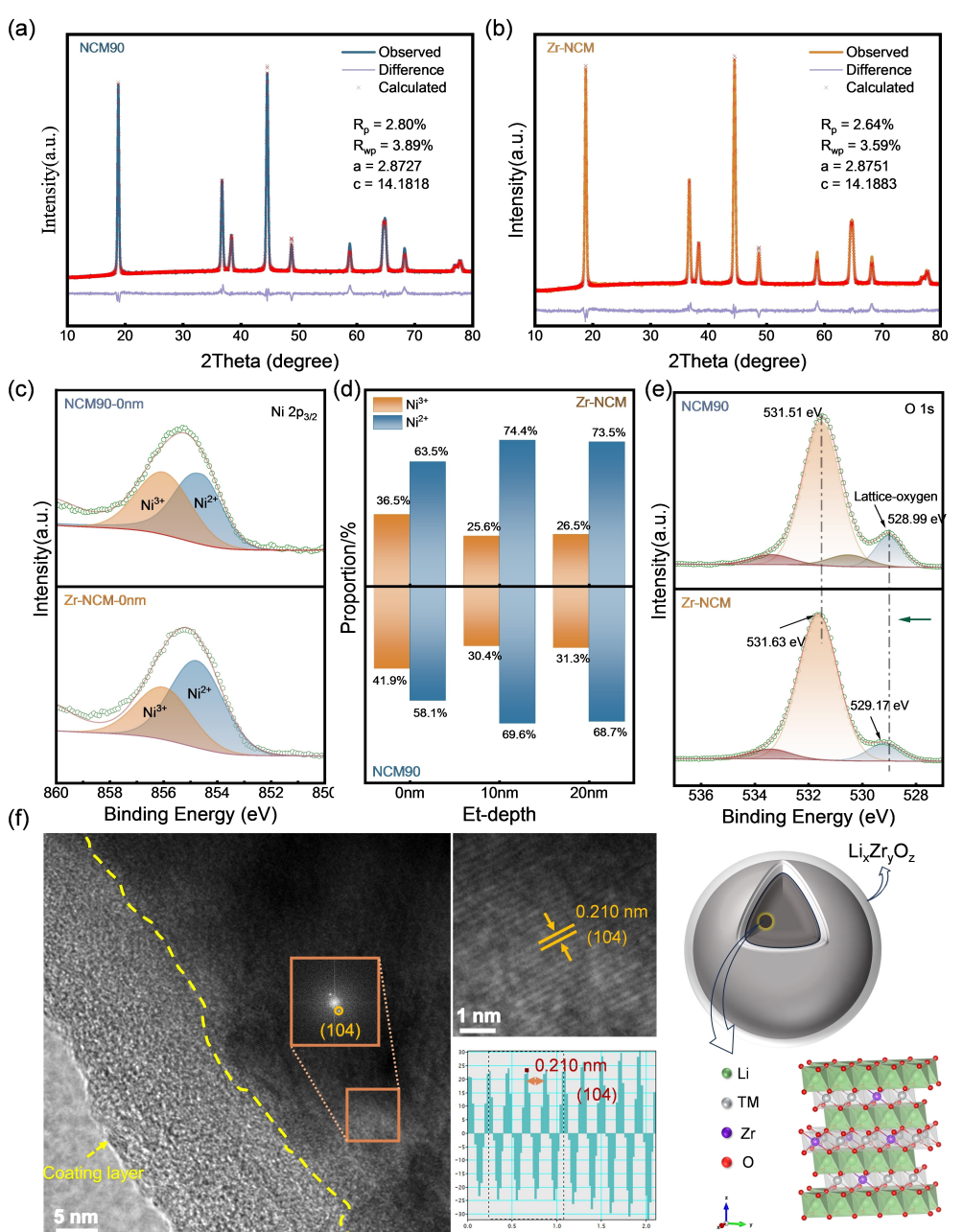


Figure 2. Rietveld refinements of XRD patterns for NCM90 (a) and Zr-NCM (b); (c) XPS patterns of Ni 2p; (d) Comparison of content of Ni^{2+} and Ni^{3+} at different depths; (e) XPS patterns of O 1s at surface of NCM90 and Zr-NCM; HRTEM images, FFT images and schematic diagram of particle structure of Zr-NCM (f).

Zr-NCM is compared with the pristine NCM90, indicating Zr⁴⁺ with a larger radius substitutes the transition metal site. And the decrease in the proportion of Ni²⁺ in the Li⁺ layer from 6.71% to 6.19% means that the Li⁺/Ni²⁺ cation mixing of Zr-NCM is ameliorated. This may be due to the fact that Zr with a more delocalized *d* orbit partially occupies the transition metal sites, which enhances the interaction among the transition metals, thereby inhibiting the migration of divalent nickel to adjacent lithium layers.^[31] The increase of lattice parameters benefits to the transport of Li⁺ in the layered structure, and the mitigation of the cation mixing means an improvement in structural stability,^[32] which is proposed to possess better electrochemical cyclic stability.

Figure 2c shows XPS profiles of Ni 2p for NCM90 and Zr-NCM samples. There are two characteristic peaks at 856.0 eV and 854.6 eV in the Ni 2p_{3/2}, ascribing to Ni³⁺ and Ni²⁺ respectively.^[33] The content of Ni²⁺/Ni³⁺ at different etch depths was quantitatively analyzed, as shown as in Figure S3 and Figure 2d. The Ni²⁺/Ni³⁺ ratio of the Zr-NCM samples is higher than that of pristine NCM90 caused by charge compensation, thus increasing the discharge capacity. In addition, the reduction of highly reactive Ni³⁺ content helps to reduce the side reactions between the cathode and the electrolyte. The O 1s peak of Zr-NCM shifts towards higher bond energy (Figure 2e), and the obvious signal of Zr 3d loaded at 181.69 eV (Zr 3d_{5/2}) and 184.69 eV (Zr 3d_{3/2}) (Figure 1f) reveals the formation of Zr–O bonds. As the bond energy of Zr–O is stronger than that

of TM–O (TM=Ni, Co, Mn),^[34] the structural stability of the sample will be significantly improved. Figure 2f illustrates the detailed microstructure of the Zr-NCM determined by high-resolution transmission electron microscopy (HRTEM) and Fourier transform (FFT). An amorphous coating layer with thickness of about 15 nm is observed on the surface of the Zr-NCM material particles, while no coating layer present on the surface of the NCM90 particles. The presence of Li₂ZrO₃ phase in 2 at% Zr modified NCM90 sample synthesized by the same process is confirmed from the XRD pattern Figure S2. Combining with the results of XPS, it is believed that this coating layer is lithium zirconium oxide formed by the reaction of the lithium residue and Zr–O bonds on the surface during the sintering process. It has also been consistent with the literature in which Zr can react with residual lithium and form lithium zirconate when the Zr salt is used as a dopant.^[27,35] In addition, the fast Fourier transform image based on the marked region exhibits that the bulk region is a layered phase (space group R-3m). It is noting that a lattice fringe spacing of 0.210 nm is clearly observed in the bulk phase, which corresponds to the (104) plane.^[36] However, the lattice space is larger than that of NCM90,^[37] indicating the successful incorporation of Zr into NCM90.

The electrochemical performance of the Zr-NCM with various Zr content was studied (Figure S4), and the 1 at% Zr modified NCM90 sample shows the large specific capacity and stable cycling performance. As shown in Figure 3a, the initial charging and discharging curves at 0.1C (1C=200 mA g⁻¹) are

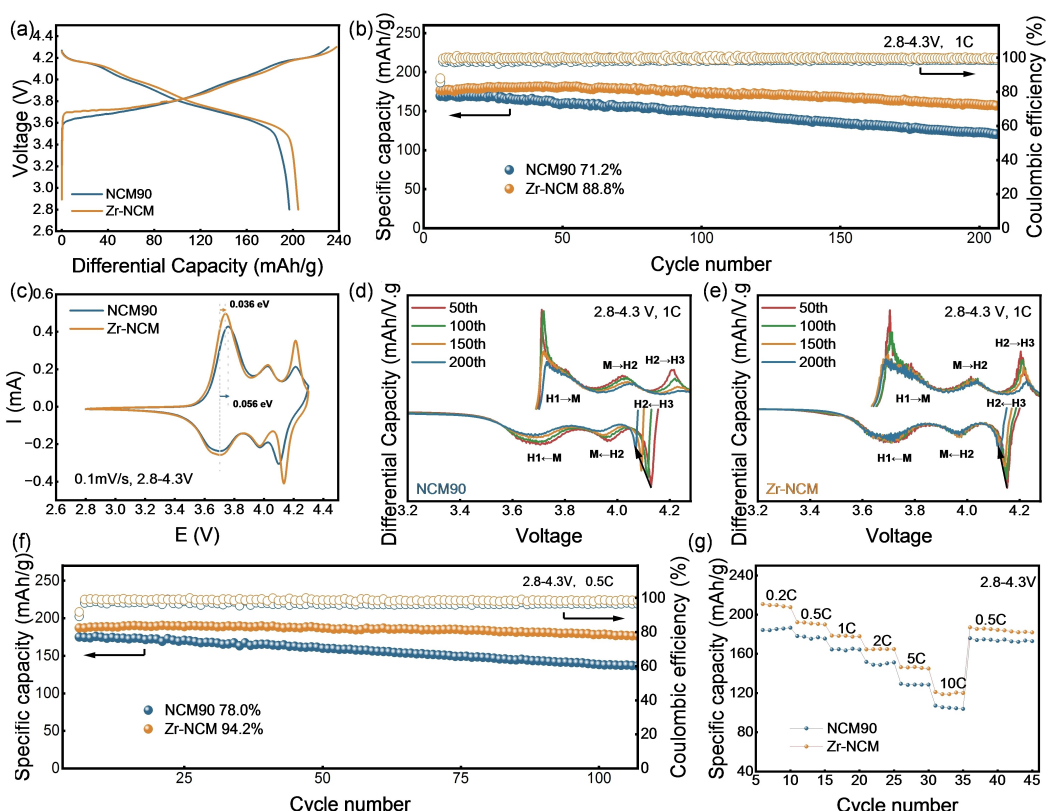


Figure 3. Initial charge–discharge curves at 0.1C (a) and the cycling performance (b) at 1C of the NCM90 and Zr-NCM conducted at 25 °C in the range of 2.8–4.3 V; (c) The cycle voltammetry curves of the initial cycle of NCM90 and Zr-NCM with a scan rate of 0.1 mV s⁻¹. The dmQ/dV profiles of the NCM90 (d) and Zr-NCM (e); Cycling performance conducted at 0.5C (f) and rate performance (g).

similar for NCM90 and Zr-NCM samples. The specific discharge capacities of NCM90 and Zr-NCM are 197.0 and 204.7 mAh g⁻¹ with the Coulombic efficiency of 85.25% and 86.07%, respectively. After 200 cycles at 1C, the Zr-NCM achieves a reversible discharge capacity of 157.0 mAh g⁻¹ with a capacity retention of 88.8%, while the pristine NCM90 delivers a reversible discharge capacity of 120.5 mAh g⁻¹ with a capacity retention of 71.2% (Figure 3b). The enhanced cycling performance of Zr-NCM stems from the improvement of the structural stability and surface coating, thereby inhibiting the internal irreversible phase transformation and reducing irreversible capacity loss. Figure 3c shows the CV curves with a scan rate of 0.1 mVs⁻¹ of the NCM90 and Zr-NCM for initial cycles. The potential difference of the initial oxidation and reduction peaks for Zr-NCM is significantly reduced compared to that of pristine NCM90, demonstrating that the Li_xZr_yO_z coating contributes to alleviate electrode polarization and improving interfacial stability. Figure 3c,d shows the dQ/dV (Q is the capacity and V is the voltage) curves for the NCM90 and Zr-NCM electrodes, which display three redox peaks corresponding to the phase transitions from hexagonal to monoclinic (H1→M), monoclinic to hexagonal (M→H2) and hexagonal to hexagonal (H2→H3), respectively. The phase transition from H2 to H3 is accompanied by a significant alteration in lattice parameter and considered to be one of the main reasons for the electrochemical irreversibility of layered oxides.^[38,39] Notably, with the increase of cycles, the phase transition peak of H2→H3 of

NCM90 decreases and widens significantly, indicating that the reversibility of phase transition is largely reduced. In contrast, the relative peaks of the Zr-NCM is more stable and the shifting moves slower, showing improved reversibility. From Figure 3f and Figure S5, the Zr-NCM shows a reversible discharge capacity of 176.6 mAh g⁻¹ after 100 cycles at 0.5C with a capacity retention of 94.2%, which is significantly higher than that of NCM90 (137.1 mAh g⁻¹, 78%, respectively). According to Figure 3g, the Zr-NCM exhibits a reversible specific capacity of 118.9 mAh g⁻¹ at 10C, while the NCM90 delivers a specific capacity of 105.5 mAh g⁻¹. The improvement in rate performance can be ascribed to the introduction of Zr–O in the bulk and the formation of the fast-ionic conductor Li_xZr_yO_z^[40,41] on the surface of NCM90 power. The incorporation of Zr–O bonds in the crystal lattice can effectively inhibit the harmful phase transition and shield the adsorption of lithium ions on to TMs (Ni, Co and Mn), which improves the structure stability and ion transport kinetics. Simutaneously, the lithium zirconium oxide coating layer formed on the surface possesses fast ionic conductivity, which can reduce the interface barrier and improve the rate performance.

GITT was used to determine the diffusion coefficients of Li⁺ during the charge-discharge process, as shown in Figure 4a. The Li⁺ diffusion coefficient of Zr-NCM is higher than that of NCM90, particularly at the end of charge and discharge regions. This confirms that the incorporation of Zr brings quickly Li⁺ diffusion kinetics, due to the large ion radius of Zr⁴⁺ enlarging

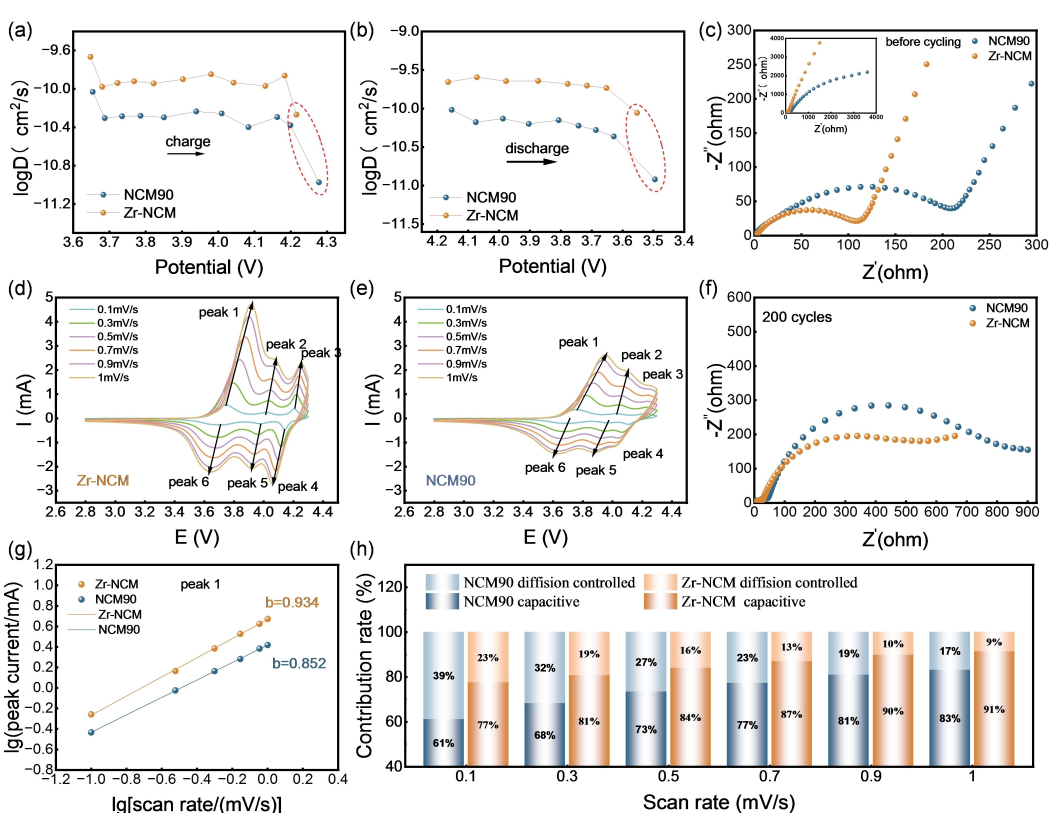


Figure 4. GITT profiles obtained during charge (a) and discharge (b) process of NCM90 and Zr-NCM; Nyquist plots of electrodes before cycling (c) and after 200 cycles (f); CV profiles of Zr-NCM (d) and NCM90 (e) at different scan rates between 2.8 and 4.3 V; (g) Linear relationship between maximum peak current (peak 1) of charge and logarithm of scan rate; (h) Capacitance contribution calculations of both samples at various scan rates.

the lattice space of NCM90. Figure 4c,f show Nyquist plots of the NCM90 and Zr-NCM before and after cycling. The obvious impedances difference of the two electrode materials further verifies that Zr-NCM90 possesses enhanced Li^+ migration efficiency, reducing the interface resistance and inhibiting the degradation of the surface structure of NCM90 during cycling. To analyze the capacity origin of the electrode materials, we checked the CV curves under various scan rates, as shown in Figure 4d,e. The Zr-NCM shows sharper and better symmetrical redox peaks, which reveals a faster electrochemical reaction process, indicating that the Zr-NCM has improved Li-ion transport kinetics and more stable structure. From Figure 4g, the b values of Zr-NCM and NCM90 are 0.934 and 0.852, respectively, which are calculated based on the maximum peak current (peak 1) in Figure S6, indicating that both electrode materials have pseudo-capacitance contribution and rapid diffusion-controlled current response attributed from the nanoscale primary particles.^[42,43] It is notably that the pseudo-capacitance contribution of Zr-NCM is higher than that of NCM90 (Figure 4h), which may be due to that the formation of the fast

ionic conductor $\text{Li}_x\text{Zr}_y\text{O}_z$ promotes the surface reaction kinetics. This result indicates that the increased rate performance of Zr-NCM comes from the promoted Li^+ diffusion kinetics.

Figure 5 shows the 2D contour plots of *in situ* XRD patterns of Zr-NCM and pristine NCM90 recorded during the second cycle at 0.1 C (Figure 5a,b). As the charging voltage increases, the Li^+ are extracted gradually, the (003) peak gradually shifts to a lower angle, indicating that the crystal lattice expands along the *c*-axis, which corresponds to the phase transition from H1 to H2 induced by the columbic repulsion between the adjacent oxygen layers.^[26,44] When the voltage reaches about 4.1 V, the (003) peak moves to the lowest angle. As the voltage further rises, the (003) peak suddenly moves to a higher angle until it reaches a largest angle of about 4.3 V, indicating that the lattice contracts sharply along the *c*-axis. This is due to the phase transition from H2 to H3, in which the interslab distance shrinks sharply along the *c*-axis due to the dissipation of charge density of oxygen ions coordinated with highly oxidized transition metal ions in a highly delithiated state. Zr-NCM has a slightly smaller H2 to H3 transition platform, which has a 0.47°

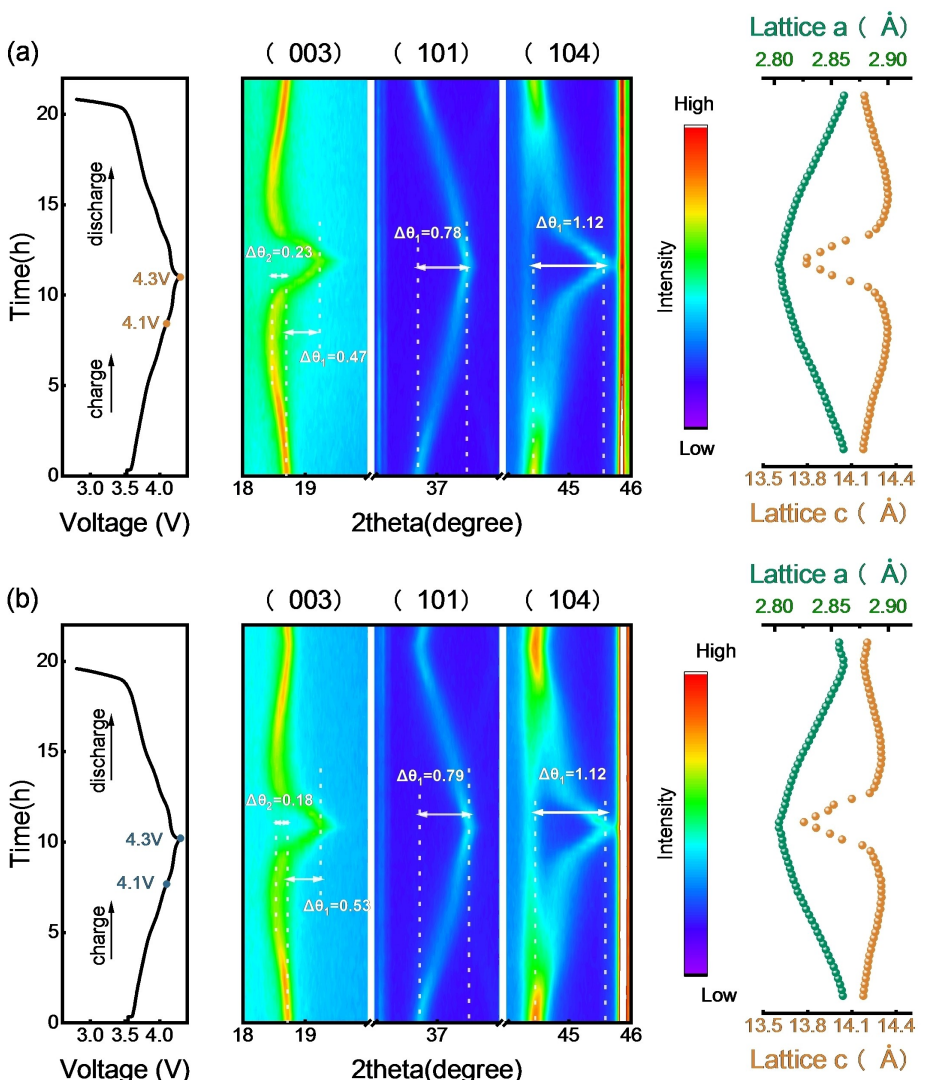


Figure 5. *In situ* XRD characterization for Zr-NCM (a) and pristine NCM90 (b) cathodes during the second cycle within 2.8–4.3 V.

between the largest angle and the initial angle, and 0.23° difference between the smallest angle and the initial angle of (003) peak (Figure 5a). In contrast, the corresponding differences for NCM90 are 0.53° and 0.18°, respectively (Figure 5b). This is because that Zr doping in the bulk with Zr–O bonding sustains the lattice, which is not only benefits to uniform detract of Li ions, but also inhibits the lattice collapse in the highly delithiated state.

Figure 6a shows the XRD patterns evolution of the Zr-NCM and pristine NCM90 electrodes before and after 200 cycles at 1C. Compared to pristine NCM90, the (003) peak of Zr-NCM moves less after cycling, which verifies that Zr–O bonding and $\text{Li}_x\text{Zr}_y\text{O}_z$ coating effectively alleviates the volume shrinkage and expansion during charge-discharge cycling (Figure 6b). Differential scanning calorimetry (DSC) was performed to evaluate the thermal stability of the NCM90 and Zr-NCM sample, which is shown in Figure 6c. The Zr-NCM exhibits better thermal stability, with an exothermic peak at 213°C and a heat generation of 1538 J g⁻¹, while the NCM90 has an exothermic peak at a lower 210.9°C with a heat generation of 2092 J g⁻¹. This result reveals that Zr-NCM possesses a more stable lattice structure caused by the Zr–O modification. Figure 6d,e display the cross-section scanning electron microscopy (SEM) images of the both cathodes after 200 cycles at 1C. There are obvious

microcracks in the pristine NCM90 (Figure 6d), while the Zr-NCM (Figure 6e) retains relatively good integrity, confirming its mechanical stability. HRTEM was performed to study the crystal structure changes of NCM90 and Zr-NCM after 200 cycles at 1C, as shown in Figure 6g,h. The NCM90 exhibits a spinel-rock salt transition region from the subsurface to the surface. In contrast, the Zr-NCM remains a good layered structure with a clear lattice fringe from the subsurface to the surface, demonstrating that Zr–O bonding effectively suppresses the irreversible transformation of surface structure. Furthermore, Figure 6f,i show the F 1s XPS profile of the NCM90 and Zr-NCM electrode surface after 200 cycles at 1C. There are two characteristic peaks at 684.56 eV and 686.85 eV in the F 1s, belonging to LiF and $\text{Li}_x\text{PO}_y\text{F}_z$ respectively.^[22,45] The less LiF in the Zr-NCM reflects that there are fewer surface side reactions, which is contributed from the $\text{Li}_x\text{Zr}_y\text{O}_z$ coating layer and pinned lattice structure. All the results above confirm that Zr-NCM exhibits superior structure stability during charge-discharge cycling.

Conclusions

In this work, a covalent pinned strategy is employed to improve the structure stability of NCM90 layered oxide cathode. Zr is

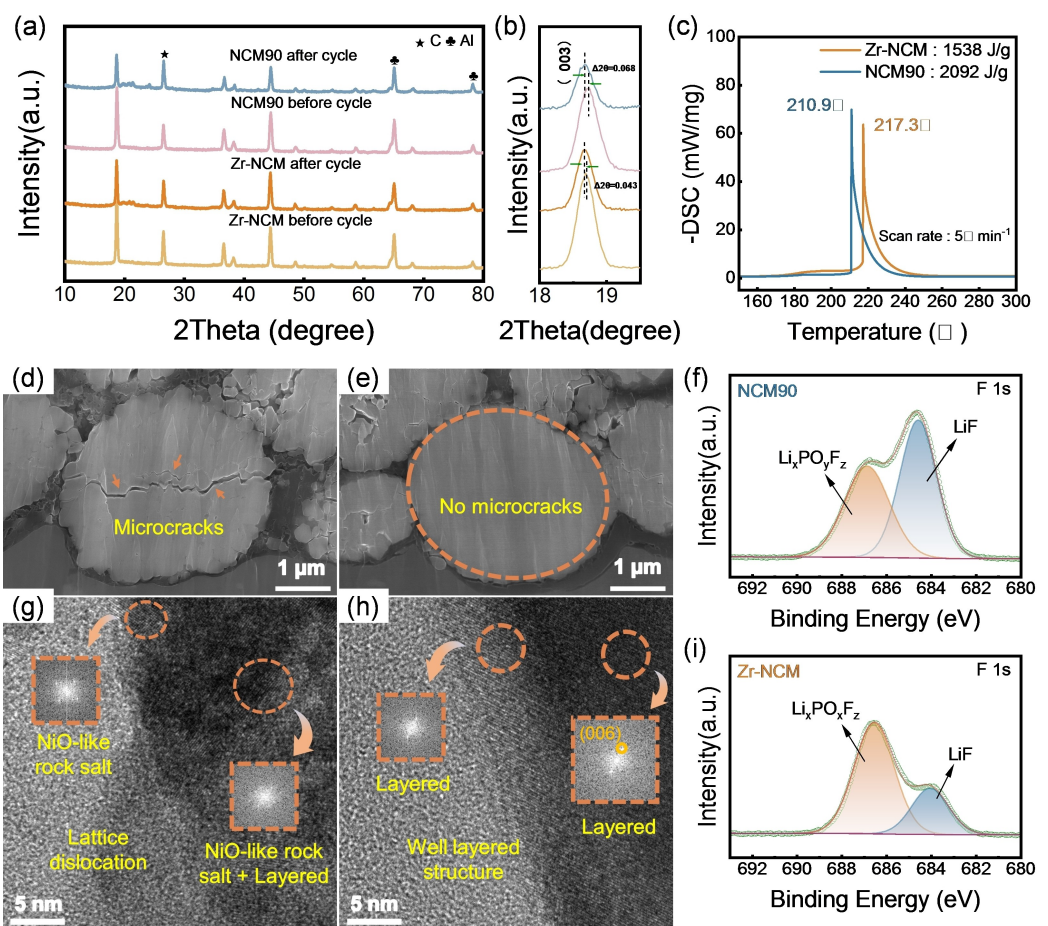


Figure 6. XRD patterns (a) and magnified view of the (003) peak (b); (c) Differential scanning calorimetry profiles of the NCM90 and Zr-NCM charged to 4.3 V. SEM images, HRTEM images, and F 1s spectrum for NCM90 (d,g,f) and Zr-NCM (e,h,i) after 200 cycles at 1C.

in situ incorporated into NCM90 during the synthesis process, which can form Zr–O covalent bonds inside the NCM90 crystal lattice and $\text{Li}_x\text{Zr}_y\text{O}_z$ coating layer on the surface of NCM90. Zr–O bonding like pinning centers can fix the crystal lattice and alleviate the Ni ions diffusion during charge-discharge process due to the stronger binding energy than that of TM(Ni, Co and Mn)-O bonds, leading to enhanced structure stability. Meanwhile, the $\text{Li}_x\text{Zr}_y\text{O}_z$ coating layer with enhanced ion conductivity ensures fast lithium ions transport crossing the crystal interface, and also effectively inhibits the occurrence of side reactions. As a result, Zr-NCM delivers a reversible discharge capacity of 201.8 mAh/g in the initial cycle between 2.8 and 4.3 V at 0.1 C, and a superior capacity retention of 88.8% after 200 cycles at 1 C, far surpassing that of initial $\text{LiNi}_{0.9}\text{Co}_{0.06}\text{Mn}_{0.04}\text{O}_2$ (78% and 72.2%, respectively). This study demonstrates that the covalent bonding strategy can effectively stabilize the structure of ultra-Ni cathode, which provides a guidance for the structure design of high-performance cathode for LIBs.

Experimental Section

Material Synthesis

The pristine $\text{LiNi}_{0.9}\text{Co}_{0.06}\text{Mn}_{0.04}\text{O}_2$ powers (NCM90) were synthesized by solid-state reaction using the oxide precursor ($\text{Ni}_{0.9}\text{Co}_{0.06}\text{Mn}_{0.04}(\text{OH})_2$, purchased from CNGR Co., Ltd.) and lithiation reagent (LiOH) as raw materials. The precursor powders were mixed in a molar ratio of 1:1.02 (transition metal: Li), which were then calcinated in a high-purity O_2 atmosphere at 450 °C for 5 h and 725 °C for 10 h to obtain $\text{LiNi}_{0.9}\text{Co}_{0.06}\text{Mn}_{0.04}\text{O}_2$.

The Zr incorporated NCM power was prepared via a pre-mixing process, and followed by a lithiation sintering process. At first, the oxide precursor and 1 at% $\text{ZrO}(\text{NO}_3)_2 \cdot x\text{H}_2\text{O}$ were added to a solution mixed with 5:1 volume ration of ethanol and deionized water, and then stirred continuously at 70 °C until the solvent was evaporated, which were dried overnight at 70 °C. Finally, the composite precursors and LiOH were mixed in a mortar (TM:Li = 1:1.04). The mixture was sintered at 450 °C for 5 h and 725 °C for 10 h under flowing high-purity oxygen.

Analytical Techniques

The crystal structure of the samples was determined by X-ray diffraction (XRD, Bruker D8, Cu K α radiation) over the 2 θ value range of 10–80° with a scan rate of 5°/min. And Rietveld refinement was performed using the Topas software. Scanning electron microscopy (SEM) and transmission electron microscopy (TEM) were performed based on Hitachi S-4800 and JEOL JEM-F200, respectively. The distribution of elements was analyzed by energy-dispersive spectrometer (EDS), and the elemental composition information was obtained by X-ray photoelectron spectroscopy (XPS, Thermo Scientific ESCALAB 250Xi).

Electrochemical Measurement

The electrochemical tests were conducted using a coin-type 2032R half-cell at room temperature. The 80 wt% active materials, 10 wt% polyvinylidene fluoride (PVDF) and 10 wt% super C45 (conducting additive) were mixed in N-methyl-2-pyrrolidone to form a slurry, which was then coated on aluminum foil and dried at 100 °C in a

vacuum oven for 8 h. Subsequently, the electrode with a thickness of about 20 μm was cut into discs with a diameter of 11 mm and an active substance mass of 2–3 mg. CR-2032-type coin cells were assembled in an argon-filled glove box ($\text{H}_2\text{O} < 0.1 \text{ ppm}$, $\text{O}_2 < 0.1 \text{ ppm}$) with a polypropylene monolayer (PP) separator and lithium metal for the counter electrode. The electrolyte was 1.2 M LiPF6 in mixture of EC:DEC:DMC (1:1:1 by volume ratio) with 1 wt% VC. Galvanostatic cycling was measured at 2.8–4.3 V using Neware system at a series of current densities ($1 \text{ C} = 200 \text{ mA g}^{-1}$). In addition, cyclic voltammetry (CV) and galvanostatic intermittent titration technique (GITT) were performed at 2.8–4.3 V. Electrochemical impedance spectroscopy (EIS) was performed at a frequency range of 0.01 Hz–100KHz. *In situ* XRD testing was performed at 0.1 C and a potential range of 2.8–4.3 V, with a scan range of 10–70° and a scan rate of 3°/min. The *in situ* cell was assembled in a glove box in the order of cathode, separator, electrolyte and lithium metal. By the way, the separator and electrolyte used are the same as those used in the coin cells.

Supporting Information

Supporting Information is available from the Wiley Online Library or from the author.

Acknowledgements

We thank the financial support from the Beijing Natural Science Foundation of China (Z230018), National Science Foundation of China (No. 52207250, 52107234), and Shandong Provincial Natural Science Foundation, China (ZR2021QE012).

Conflict of Interests

The authors declare no conflict of interest.

Data Availability Statement

The data that support the findings of this study are available from the corresponding author upon reasonable request.

Keywords: covalent pinning effect · Zr–O bonding · NCM90 · $\text{Li}_x\text{Zr}_y\text{O}_z$ · structure stability

- [1] W. Li, E. M. Erickson, A. Manthiram, *Nat. Energy* **2020**, *5* (1), 26–34.
- [2] R. Schmuck, R. Wagner, G. Horpel, T. Placke, M. Winter, *Nat. Energy* **2018**, *3* (4), 267–278.
- [3] A. Manthiram, *Nat. Commun.* **2020**, *11* (1), 1550–1550.
- [4] C.-H. Jung, H. Shim, D. Eum, S.-H. Hong, *J. Korean Ceram. Soc.* **2021**, *58* (1), 1–27.
- [5] M. Li, T. Liu, X. Bi, Z. Chen, K. Amine, C. Zhong, J. Lu, *Chem. Soc. Rev.* **2020**, *49* (6), 1688–1705.
- [6] A. Manthiram, B. Song, W. Li, *Energy Storage Mater.* **2017**, *6*, 125–139.
- [7] H.-J. Noh, S. Youn, C. S. Yoon, Y.-K. Sun, *J. Power Sources* **2013**, *233*, 121–130.
- [8] H.-H. Ryu, K.-J. Park, C. Yoon, Y.-K. Sun, *Chem. Mater.* **2018**, *30* (3), 1155–1163.

- [9] G.-L. Xu, X. Liu, A. Daali, R. Amine, Z. Chen, K. Amine, *Adv. Funct. Mater.* **2020**, *30* (46), 2004748-n/a.
- [10] X. Wang, Y.-L. Ding, Y.-P. Deng, Z. Chen, *Adv. Energy Mater.* **2020**, *10* (12), 1903864-n/a.
- [11] X. Wang, Y. Bai, X. Wang, C. Wu Chin, *J. Chem.* **2020**, *38* (12), 1847–1869.
- [12] S. Zhang, *Energy Storage Mater.* **2020**, *24*, 247–254.
- [13] M. Li, J. Lu, *Science* **2020**, *367* (6481), 979–980.
- [14] Q. Lin, W. Guan, J. Meng, W. Huang, X. Wei, Y. Zeng, J. Li, Z. Zhang, *Nano Energy* **2018**, *54*, 313–321.
- [15] S. Yin, W. Deng, J. Chen, X. Gao, G. Zou, H. Hou, X. Ji, *Nano Energy* **2021**, *83*, 105854.
- [16] L. Ni, S. Zhang, A. Di, W. Deng, G. Zou, H. Hou, X. Ji, *Adv. Energy Mater.* **2022**, *12* (31), 2201510-n/a.
- [17] H. Sheng, X.-H. Meng, D.-D. Xiao, M. Fan, W.-P. Chen, J. Wan, J. Tang, Y.-G. Zou, F. Y. Wang, R. Wen, J.-L. Shi, Y.-G. Guo, *Adv. Mater.* **2022**, *34*(12), e2108947.
- [18] J. Sicklinger, M. Metzger, H. Beyer, D. Pritzl, H. A. Gasteiger, *J. Electrochem. Soc.* **2019**, *166* (12), A2322–A2335.
- [19] X. Wang, D. Ren, H. Liang, Y. Song, H. Huo, A. Wang, Y. Gao, J. Liu, Y. Gao, L. Wang, X. He, *Energy Environ. Sci.* **2023**, *16* (3), 1200–1209.
- [20] C. Li, W. Kan, H. Xie, Y. Jiang, Z. Zhao, C. Zhu, Y. Xia, J. Zhang, K. Xu, D. Mu, F. Wu, *Adv. Sci.* **2019**, *6* (4), 1801406-n/a.
- [21] J. Li, W. Zhong, Q. Deng, Q. Zhang, Z. Lin, C. Yang, *Adv. Funct. Mater.* **2023**, *33* (24), 2300127-n/a.
- [22] Z. Tan, X. Chen, Y. Li, X. Xi, S. Hao, X. Li, X. Shen, Z. He, W. Zhao, Y. Yang, *Adv. Funct. Mater.* **2023**, *33* (26), 2215123.
- [23] Y. Chu, Y. Mu, L. Zou, Y. Hu, J. Cheng, B. Wu, M. Han, S. Xi, Q. Zhang, L. Zeng, *Adv. Mater.* **2023**, *35* (21), e2212308.
- [24] J.-L. Shi, R. Qi, X.-D. Zhang, P.-F. Wang, W.-G. Fu, Y.-X. Yin, J. Xu, L.-J. Wan, Y.-G. Guo, *ACS Appl. Mater. Interfaces* **2017**, *9* (49), 42829–42835.
- [25] W. Zhou, H. Huang, X. Liu, J. Gao, S.-M. Hao, Y. Yang, J. Qiu, *Adv. Energy Mater.* **2023**, *13* (32), n/a-n/a.
- [26] J. Li, H. Yang, Q. Deng, W. Li, Q. Zhang, Z. Zhang, Y. Chu, C. Yang, *Angew. Chem. Int. Ed.* **2024**, *136* (10), n/a-n/a. 10.1002/ange.202318042.
- [27] L. Yao, Y. Li, X. Gao, M. Cai, J. Jin, J. Yang, T. Xiu, Z. Song, M. E. Badding, Z. Wen, *Energy Storage Mater.* **2021**, *36*, 179–185.
- [28] T. He, Y. Lu, Y. Su, L. Bao, J. Tan, L. Chen, Q. Zhang, W. Li, S. Chen, F. Wu, *ChemSusChem* **2018**, *11* (10), 1639–1648.
- [29] H. Yang, H.-H. Wu, M. Ge, L. Li, Y. Yuan, Q. Yao, J. Chen, L. Xia, J. Zheng, Z. Chen, J. Duan, K. Kisslinger, X. Zeng, W.-K. Lee, Q. Zhang, J. Lu, *Adv. Funct. Mater.* **2019**, *29* (13), 1808825-n/a.
- [30] Z. Feng, R. Rajagopalan, S. Zhang, D. Sun, Y. Tang, Y. Ren, H. Wang, *Adv. Sci.* **2021**, *8* (2), 2001809-n/a.
- [31] H.-X. Wei, L.-B. Tang, Y.-D. Huang, Z.-Y. Wang, Y.-H. Luo, Z.-J. He, C. Yan, J. Mao, K.-H. Dai, J.-C. Zheng, *Mater. Today* **2021**, *51*, 365–392.
- [32] S. F. Amalraj, R. Raman, A. Chakraborty, N. Leifer, R. Nanda, S. Kunnikuruvan, T. Kravchuk, J. Grinblat, V. Ezersky, R. Sun, F. L. Deepak, C. Erk, X. Wu, S. Maiti, H. Sclar, G. Goobes, D. T. Major, M. Talianker, B. Markovsky, D. Aurbach, *Energy Storage Mater.* **2021**, *42*, 594–607.
- [33] Y. Zou, X. Yang, C. Lv, T. Liu, Y. Xia, L. Shang, G. I. N. Waterhouse, D. Yang, T. Zhang, *Adv. Sci.* **2017**, *4* (1), 1600262.
- [34] D. Wang, X. Li, Z. Wang, H. Guo, Y. Xu, Y. Fan, J. Ru, *Electrochim. Acta* **2016**, *188*, 48–56.
- [35] S. Gao, X. Zhan, Y.-T. Cheng, *J. Power Sources* **2019**, *410*, 45–52.
- [36] J. Li, M. Zhang, D. Zhang, Y. Yan, Z. Li, *Chem. Eng. J.* **2020**, *402*, 126195.
- [37] Z.-Z. Yu, G.-Q. Zhao, F.-L. Ji, H. Tong, H.-C. Li, Y. Cheng, *Rare Met.* **2023**, *42* (12), 4103–4114.
- [38] Z. Feng, R. Rajagopalan, D. Sun, Y. Tang, H. Wang, *Chem. Eng. J.* **2020**, *382*, 122959.
- [39] L. Wang, T. Liu, T. Wu, J. Lu, *Nature* **2022**, *611* (7934), 61–67.
- [40] Y. V. Baklanova, I. Y. Arapova, A. L. Buzlukov, A. P. Gerashenko, S. V. Verkhovskii, K. N. Mikhalev, T. A. Denisova, I. R. Shein, L. G. Maksimova, *J. Solid State Chem.* **2013**, *208*, 43–49.
- [41] B. Song, W. Li, S.-M. Oh, A. Manthiramet, *ACS Appl. Mater. Interfaces* **2017**, *9* (11), 9718–9725.
- [42] X. Yang, A. L. Rogach, *Adv. Energy Mater.* **2019**, *9* (25), 1900747.
- [43] F. Lu, Y. Ji, D. Shi, J. Yao, L. Pei, *J. Colloid Interface Sci.* **2023**, *641*, 510–520.
- [44] X.-H. Meng, X.-D. Zhang, H. Sheng, M. Fan, T. Lin, D. Xiao, J. Tian, R. Wen, W.-Z. Liu, J.-L. Shi, L.-J. Wan, Y.-G. Guo, *Angew. Chem. Int. Ed.* **2023**, *135* (22), n/a-n/a. 10.1002/ange.202302170.
- [45] L. Mu, Z. Yang, L. Tao, C. K. Waters, Z. Xu, L. Li, S. Sainio, Y. Du, H. L. Xin, D. Nordlund, F. Lin J Mater, *Chem. A* **2020**, *8* (34), 17487–17497.

Manuscript received: April 1, 2024
Revised manuscript received: May 10, 2024
Accepted manuscript online: May 18, 2024
Version of record online: June 18, 2024